Infrared thermography with non-uniform heat flux boundary conditions on the rotor endwall of an axial turbine

Infrared thermography with non-uniform heat flux boundary conditions on the rotor endwall of an axial turbine

S Lazzi Gazzini[1]**, R Schädler**[1]**, A I Kalfas**[2] **and R S Abhari**[1]

[1] Laboratory for Energy Conversion, Department of Mechanical and Process Engineering, ETH Zürich, ML J 33, Sonneggstrasse 3, CH-8092, Zürich, Switzerland
[2] Department of Mechanical Engineering, Aristotle University of Thessaloniki, 54124 Thessaloniki, Greece

E-mail: lazzigas@ethz.ch

Abstract

It is technically challenging to measure heat fluxes on the rotating components of gas turbines, yet accurate knowledge of local heat loads under engine-representative conditions is crucial for ensuring the reliability of the designs. In this work, quantitative image processing tools were developed to perform fast and accurate infrared thermography measurements on 3D-shaped film-heaters directly deposited on the turbine endwalls. The newly developed image processing method and instrumentation were used to measure the heat load on the rotor endwalls of an axial turbine. A step-transient heat flux calibration technique is applied to measure the heat flux generated locally by the film heater, thus eliminating the need for a rigorously iso-energetic boundary condition. On-board electronics installed on the rotor record the temperature readings of RTDs installed in the substrate below the heaters in order to evaluate the conductive losses in the solid. Full maps of heat transfer coefficient and adiabatic wall temperature are produced for two different operating conditions, demonstrating the sensitivity of the technique to local flow features and variations in heat transfer due to Reynolds number effect.

Keywords: turbomachinery, infrared thermography, heat transfer, image processing

(Some figures may appear in colour only in the online journal)

List of symbols

A_{ew}	Endwall surface area (mm^2)		p_1	Linear fit coefficient (slope) (K $(\sqrt{s})^{-1}$)
C_{ax}	Axial chord of rotor blade at midspan (mm)		p_2	Linear fit coefficient (intercept) (K)
C_p	Specific heat at constant pressure (J $(kg \cdot K)^{-1}$)		P	Electrical power (W)
d	Thickness of heating film (μm)		$\dot{q}''$	Heat flux (W m^{-2})
D	Thickness of substrate (mm)		s	Sharp image
e	Thermal effusivity (J $\cdot$ K $\cdot \sqrt{s}$ m^{-2})		S_q	Heat flux scaling factor (-)
h	Heat transfer coefficient (W $(m^2 \cdot K)^{-1}$)		St	Stanton number (-)
i	Electric current (A)		SSIM	Structure similarity index (-)
k	Blur kernel		t	Time (s)
n	Number of iterations (-)		T	Temperature (K)
MSSIM	Mean structure similarity index (-)		v	Rotor-relative flow velocity (m s^{-1})
Nu	Nusselt number (-)		w	Width of heating track (mm)
			x	Position vector (m)
			y	Blurred image

Greek

α	Thermal diffusivity (m^2 s^{-1})
δ	Density of the substrate (kg m^{-3})
ε	Emissivity (-)
Θ	Non-dimensional temperature (-)
κ	Thermal conductivity (W (m $\cdot$ K)$^{-1}$)
μ	Mean intensity of the image (digital levels)
ρ	Electrical resistivity of the film ($\Omega \cdot$ m)
σ	Stefan–Boltzmann constant (W (m$^2 \cdot$ K^4)$^{-1}$]
τ	Thermal diffusivity time constant (s)

Subscripts

∞	Property of the mean flow
0	Initial value
air	Property of air
ad	Adiabatic wall temperature
cond	Conductive heat flux
conv	Convective heat flux
el	Heat flux produced by electrical heater
ew	Endwall
in	Value at inlet
opt	Optimal number of iterations
paint	Property of the high-emissivity coating
rad	Radiative heat flux
rel	In the rotor-relative frame of reference
sub	Property of the PEEK substrate
t	Total temperature
w	Wall temperature

1. Introduction

Infrared thermography is a versatile, non-intrusive temperature measurement technique returning remarkable data density. It is employed in very diverse applications, such as medical science, non-destructive testing and environmental science, as exhaustively reported by Meola *et al* [1] and Carlomagno *et al* [2]. In the field of thermo-fluid-dynamics, infrared thermography is used to measure convective heat transfer both at a fundamental level (Scherer *et al* [3]) and in more application-oriented contexts (Schulz [4]). Application of the technique to rotating machinery or components is of interest for a variety of fields (fundamental fluid mechanics, Cardone *et al* [5]; automotive, Lyons *et al* [6]; railway engineering, Siroux *et al* [7]), but limitations in the acquisition speed of the detector typically allow quantitative measurements only in a circumferentially averaged fashion. An attempt to reconstruct a full temperature map of a rapidly rotating disk is reported in 2002 by Astarita *et al* [8]. The objective of their work is to visualize and count the spiral vortices formed by the rotation of the surface of the disk. Their ingenious, purely geometrical reconstruction provides enough qualitative detail of the temperature field to visualize the signatures of the vortices, but cannot be used to infer quantitative heat transfer measurements due to the smearing of the temperature profiles. In fact, quantitative information on the surface heat loads on a similar setup, but with the addition of a jet, is provided later in 2008 by the same group, but still in an azimuthally averaged fashion (Astarita *et al* [9]).

Gas turbine engine efficiency is typically improved by increasing the maximum temperature of the thermodynamic cycle (Dunn [10],). More severe thermal loads, on the other hand, impact the life of the components, unless they are cooled more effectively. An accurate knowledge of the local surface temperatures and heat transfer coefficients enables the design of bespoke cooling schemes and a more realistic lifing of the part, thus contributing to the enhancement of the engine's performance and durability.

Numerical predictions provide high-density information, but require experimental validation under engine-representative conditions. Given the highly complex flow in a turbine passage, a validation performed on full maps of heat transfer coefficient and adiabatic wall temperature can more thoroughly confirm the accuracy of the prediction tools used. Additionally, resolving the thermal gradients enables the evaluation of the local material stresses acting on the part.

Two- and three-dimensional data are nowadays almost routinely acquired in linear and annular cascades. However the effects induced by rotation, such as bulk forces and unsteady rotor/stator interaction, cannot be easily simulated in stationary facilities. Furthermore, these effects influence the heat transfer in ways that are not always possible to decouple (Dunn [10]), hence the need for measurements performed directly on the rotating components.

Blair's [11] work is one of the earliest attempts to measure heat transfer in rotating facilities. His technique employed foil heaters and arrays of thermocouples soldered to their surface to measure aerofoil and endwall heat transfer on a large-scale, low-speed rotating facility. Contours of heat transfer coefficient and adiabatic wall temperature were determined by joining the values measured at the thermocouple locations. Heat flux gauges have been successfully and reliably employed in short-duration facilities. de la Loma *et al* [12] provide a concise list of works of this kind. In particular, the works by Abhari [13] and Dunn [14, 15] are worth a special mention. In these papers, the accuracy of the results and the representativeness of the operating conditions with respect to true engine operation are remarkable, but data are only provided at discrete locations on the aerofoils and endwalls of stators and rotors.

Moffat [16] describes broad-band liquid crystals thermography and infrared thermography as the only two experimental techniques able to provide full maps of heat transfer coefficient and adiabatic wall temperature. Significant improvements have been made in the accuracy and speed of commercially available infrared imaging systems, especially after the introduction of 3rd generation infrared detectors in the early 2000s (Rogalski [17]). Nowadays it is possible to purchase devices capable of measuring temperatures with integration times in the order of tens of microseconds in the long-wave infrared range. Still, signal to noise ratio limitations restrict the possibility of applying such devices for the measurements of heat transfer in the rotating frame of reference of 'cold' (i.e. close to ambient temperature) high-speed or even moderate speed turbine facilities.

Essentially, the main challenges of measuring on the rotor of a turbine by means of infrared thermography can be summarized as follows:

- limitations on the integration time of the camera under the contrasting requirements of a sufficiently high signal-to-noise ratio and of being able to acquire a sharp image of a rapidly moving object;
- implementation of an accurately known thermal boundary condition with instrumentation able to withstand the centrifugal loads;

The current work focuses on new tools and methods developed to overcome these challenges through:

- new, frequency-based infrared thermogram composition, enabling accurate infrared imaging at high speeds and with high spatial resolution (section 3);
- the development of a manufacturing process to produce a film heater on virtually any complex endwall geometry;
- the development of a technique to measure the locally provided heat flux from the newly produced film heater (section 2.2).

Proof-of-concept results are presented from measurements performed in a moderate-speed, rotating axial turbine research facility at the Laboratory for Energy Conversion at ETH Zürich.

The heat transfer coefficient and adiabatic wall temperature distributions observed are related to flow features expected in the rotor endwall passage. The image processing tools and calibration procedures developed for this work, despite having being tested in the specific environment of an axial turbine, are transferrable to any setup involving rapidly moving objects requiring short integration times for the IR detectors. Additionally, the fabrication of a 3D-shaped, directly deposited, robust film heater enables the application of the experimental method to complex surface geometries.

2. Experimental setup

The instrumentation specific to the heat transfer measurements can be separated into stationary and rotating.

The stationary instrumentation consists of a fast infrared camera mounted on a traversing system, the power supply units to the rotating instrumentation, the power monitoring system and a data acquisition computer. Optical access to the rotor endwall is granted by three Zinc–Selenide (ZnSe) windows mounted in the rotor casing. The windows carry an anti-reflective coating that increases their transmissivity in the long-wave infrared range to 96%. More views of the hub can be acquired by traversing the camera so as to cover a wider portion of the endwall surface. Details on the infrared camera are provided in section 2.1.

The instrumentation mounted on the rotor includes a 2-channel slip ring for power transmission, a set of 9 Wi-Fi data acquisition boards and a special hub platform insert carrying a film heater and 9 embedded PT100 RTDs. A schematic of the complete setup is provided in figure 1.

In the following sections, detailed explanations of each major component of the setup are given, with particular reference to the manufacturing and calibration of the heat transfer platform.

2.1. Fast infrared camera

Imaging rapidly moving objects in the long-wave infrared range requires highly responsive infrared detectors, capable of returning sufficient signal with good signal-to-noise ratio at low integration times.

The integration time is defined as the time interval during which the detector of the infrared camera is active and building up charge as a consequence of the absorption of infrared radiation. The signal recorded by the read-out electronics is proportional to the integration time when the same amount of radiation is insisting on the pixels of the detector.

A FLIR SC7300L infrared camera is chosen for the high responsivity of its detector in the long-wave infrared range and the short, customizable integration time. This instrument features a 256×320 pixel, Mercurium–Cadmium–Telluride (HgCdTe or MCT) detector, cooled by a Stirling refrigerator at 77 K and with a pixel size of 30 μm. The integration time of the detector can be set down to 3 μs.

For the current study, two requirements were set to ensure successful heat transfer measurements on the rotor endwall of the turbine facility. They were:

- a maximum movement of the rotor endwall of 1 mm during the acquisition of a frame. This requirement translates into a maximum allowable integration time of 10 μs, based on the radius of the rotor at the hub and on the rotational speed of the turbine during the measurements;
- a maximum error in the measured temperature of 0.5 K.

The first constraint ensures that the smearing of the temperature contours does not exceed an extent of 3 pixels, given the spatial resolution of the optical setup used during the measurements (0.32 mm/pixels, see section 3.1). This is equivalent to the effect of the superposition of the 1000 frames acquired per sequence (section 4.2), which is done with a minimum tolerance on the rotor displacement of ± 1 pixel. The uncertainty on wall temperature has been described as the main driver of global heat transfer uncertainties for iso-energetic setups in previous works (Lynch *et al* [18]). This is why the second constraint strictly limits its value to match the order of magnitude indicated by Lynch *et al* themselves for their own experiment and by Laveau *et al* [19, 20] when performing IR-based heat transfer measurements in the same facility and with similar wall temperature ranges as in the present study. Based on tests performed on a black body IR source, it was found that for an integration time of 10 μs, the root mean square error in temperature over a frame at 60 °C is 0.25 °C, with peak-to-peak oscillations of ± 1 °C.

It is thus not possible to satisfy both requirements with this integration time setting. Satisfactory temperature accuracy can be obtained by increasing the integration time to 50 μs. With this setting, the noise-induced error in temperature decreases by a factor of 5. On the other hand, the movement of the rotor endwall during the integration is 5 times bigger.

The solution applied in this study is to combine the information collected in two data sets acquired with a different integration time (namely, 10 μs and 50 μs) using the image restoration procedure described in section 3.
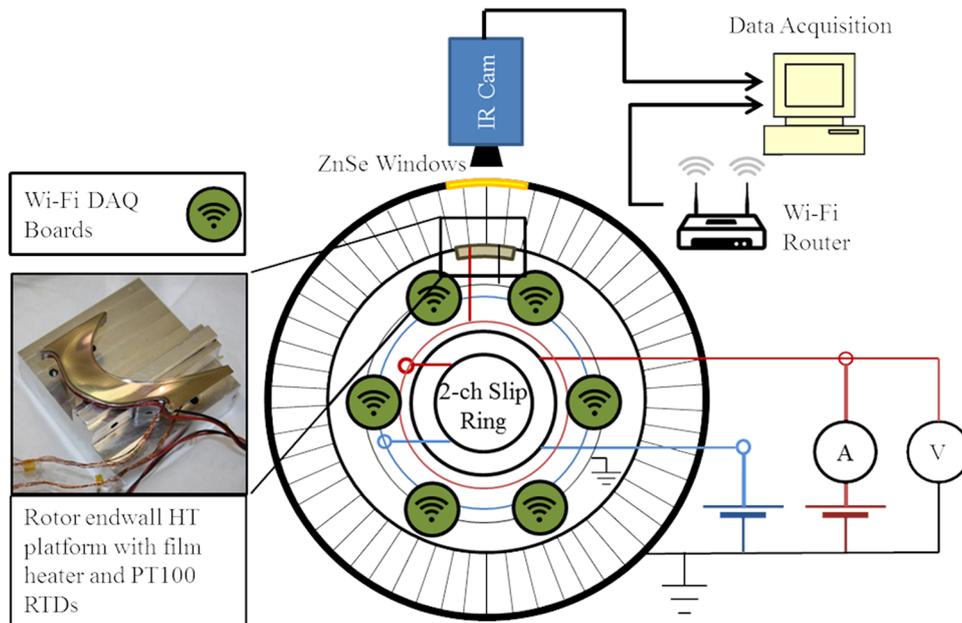
Figure 1. Schematic of the heat transfer measurement setup.

The temperature calibration of the infrared camera is performed on a test bench replicating the optical setup used in the facility—i.e. the ZnSe window and camera arrangement, respecting the relative distances within ±1 mm, by replacing the endwall heater with an isothermal black body (ISOTECH® Graybody Source 975) presenting a temperature stability of ±0.005 °C. Measurements are performed every 15 °C in the range from 30 °C to 120 °C, thus including the full range of temperatures experienced during the turbine testing. This semi *in situ* calibration method resembles the one suggested by Ochs *et al* [21].

2.2. Film heater development

A known thermal boundary condition must be applied to the endwalls in order to derive the heat transfer coefficient and adiabatic wall temperature at every point.

Direct deposition of film heaters on non-conductive substrates presents the following advantages for the application on the rotating frame:

- the low weight per unit area of the film heaters dramatically reduces centrifugal loads compared to bulk-heating devices (e.g. cartridge heaters);
- the insulating substrates can be fabricated out of light, polymeric material, as opposed to the conductive—therefore metallic—substrates required by isothermal, bulk-heated setups. This solution is, therefore, even more convenient from a mechanical standpoint;
- ~20 times lower power requirements for reaching the desired endwall temperatures under the expected convective conditions compared to isothermal solutions requiring the heating of a solid piece of conductive material;
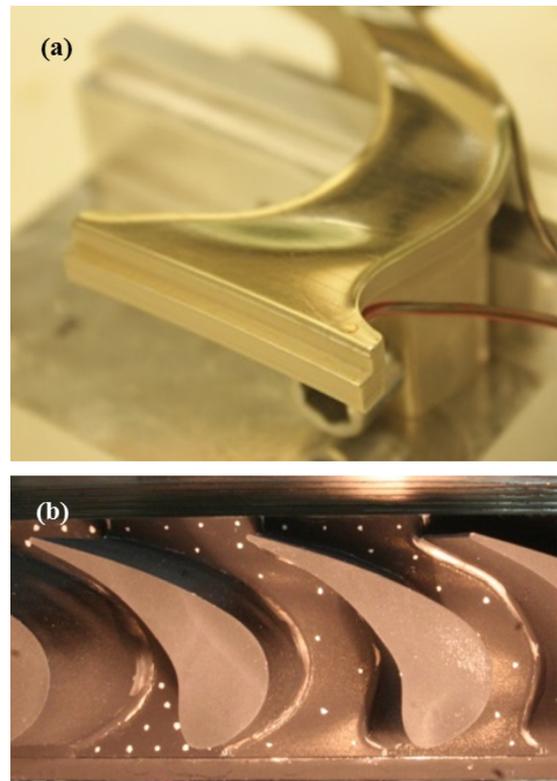- applicability of the technique to virtually any endwall geometry.

Figure 2. Heat transfer platform with directly deposited film heater before (a) and after (b) installation on the rotor blisk and application of high-emissivity coating.

Furthermore, the simple construction and strong adhesion limit the chances of failure under centrifugal loads.

The insulating substrate is shaped as a 3D hub insert (figure 2(a)) to be fit in a pocket cut out between two rotor blades to complete the hub platform (figure 2(b)). This allows instrumentation and calibration of the part prior to its installation on the rotor.

The material chosen for the construction of the hub insert is PEEK (Poly-ether-ether-ketone). Its low thermal conductivity ($\kappa = 0.25$ W m^{-1} · K^{-1}) is favourable as it contains the conduction losses through the substrate, while the good machinability allows the fabrication of pieces with complex shapes. Additionally, the material presents a sufficiently high yield strength (90 MPa), which makes it suitable for the expected loads under rotation.

The conductive material is deposited on the surface of the PEEK platform by means of e-beam physical vapour deposition. The structure of the metallic multilayer consists of a 10 nm layer of Chromium for adhesion to the organic substrate, 200 nm of Nickel and 10 nm of Gold to protect the lower layers from oxidation and allow the soldering of power connections.

The multilayer is then laser-cut into a serpentine of 1.65 mm track width (figure 3). This value of the width is calculated based on the range of target heat fluxes (~1–10 kW m^{-2}) and the following equation:

$$\dot{q}''_{\mathrm{el}} = \left(\frac{i}{w}\right)^2 \frac{\rho}{d} \qquad (1)$$

which relates width w and thickness d of the tracks, the feeding current i to the heater, the electrical resistivity ρ of the conductive film and the heat flux $\dot{q}''_{\mathrm{el}}$ produced by Joule effect. The required range of surface heat flux is estimated based on a 1D convective/conductive model. The turns of the serpentine are kept as close as possible to the fillets of the adjacent blades in order to exclude the heat flux non-uniformities coming from local current concentrations from the measurement area. An overall resistance of 533 Ω is measured for the heater at ambient temperature, corresponding to an average value of resistivity for the composite metal layer of 2.4×10^{-7} Ω · m, which is consistent with what is observed in literature for thin-film Nickel layers [22].

High-emissivity paint (emissivity value 0.98) is applied on the top surface of the heaters for the infrared thermography measurements. The thickness of the paint is measured by means of mechanical profilometry on samples that underwent the same spraying procedure and is found to be ~30 μm. The thermal resistance of the paint layer is, therefore, small compared to the one of the plastic substrate (~0.4%). Its effect on the heat transfer coefficient is negligible, as it is limited to the determination of the conductive losses and is one order of magnitude below the influence of other sources of error. Low-emissivity markers in the form of dots of silver ink are drawn on the endwall surface (figure 2(b)) to allow the projection of the images on a 130000-node 3D mesh of the endwall.

2.2.1. Step-wise transient heat flux calibration. The detrimental effect of unverified assumptions on heat flux distributions and conduction losses in the substrate are well exemplified in the recent work of O'Dowd *et al* [23], which compares the steady-state heated foil technique to other infrared-based experimental techniques. The goal of most authors relying on film or foil heaters is to obtain a uniform heat flux boundary condition, regardless of whether the surface temperature is measured with thermocouples (Blair [11], Graziani [24]), infrared thermography (Lynch [18]) or thermochromic liquid crystals (Simonich [25], Baughn *et al* [26]). Moffat [16] demonstrates analytically and verifies experimentally that the heat transfer coefficient h defined with the adiabatic wall temperature T_{ad} (equation (2)) is rigorously invariant and independent of thermal boundary conditions. It is, in fact, purely a function of geometrical and fluid mechanics parameters:

$$h = \frac{\dot{q}''_{\mathrm{conv}}}{(T_{\mathrm{w}} - T_{\mathrm{ad}})} \qquad (2)$$

Given the independence of the heat transfer coefficient to local boundary conditions, if a way is found to measure the heat flux provided by the heating device on a local basis, it would be possible to evaluate the local convective heat flux accurately, even in the presence of severe non-uniformities.

The uniformity of the locally generated heat flux can be affected by:

- thickness non-uniformities in the deposited metallic layer;
- resistivity non-uniformities in the deposited material;
- improper electrical separation between tracks after laser ablation.

A step-wise transient calibration procedure is applied in order to measure the locally generated heat flux. The method used presents similarities to the transient hot strip (THS) method developed by Gustafsson *et al* [27] in 1979. Gustafsson's method consists of heating samples of solid material by producing a uniform and known heat flux by means of a resistive rectangular strip of uniform thickness. The strip is placed in the middle of two blocks of the material, the properties of which (i.e. thermal conductivity and thermal diffusivity) are to be measured. Heat is produced by Joule effect in a step-wise transient fashion. The change in the resistance of the hot strip is measured over time and related to the local temperature increase. The temperature increase is finally compared to the analytical solution for an infinitely long planar heat source.

The key differences between the technique employed in this work and the THS method are:

- the heat source is at the surface of the solid rather than between two blocks of material. The mathematical model used for the evaluation of the heat flux is described in section 2.2.2;
- the substrate onto which the heat source lies is fully three-dimensional;
- the method is used to measure the local non-uniformity of the heat flux relative to the average heat flux value, instead of the thermal properties of the substrate.

2.2.2. Theoretical background. For a homogeneous, semi-infinite solid with a source of heat flux at its surface providing heat flux suddenly for time $t > t_0$, the temperature rise ΔT at the surface of the solid is given by:

$$\Delta T = T(t) - T_0 = \frac{2 \cdot \dot{q}''_{\mathrm{el}}}{e} \cdot \sqrt{\frac{t}{\pi}} \qquad (3)$$

Where $T(t)$ is the surface temperature at the instant t, T_0 is the initial temperature and $\dot{q}''_{el}$ is the heat flux generated by the source. By performing a linear fit of the experimental temperature rise ΔT with respect to $\sqrt{t}$, two coefficients p_1 and p_2. ΔT can be expressed as a linear function of $\sqrt{t}$:

$$\Delta T = p_1 \cdot \sqrt{t} + p_2 \tag{4}$$

It is immediately possible, then, to solve for $\dot{q}''_{el}$ by comparing equations (3) and (4):

$$\dot{q}''_{el} = \frac{\sqrt{\pi}}{2} \cdot e \cdot p_1 \tag{5}$$

Known the thermal effusivity e of the substrate, the locally produced heat flux $\dot{q}''_{el}$ can be calculated under the following assumptions:

- one-dimensionality;
- the source of heat flux is located at the free surface of the solid and in perfect thermal contact with the substrate;
- the initial temperature of the substrate is homogeneous;
- the solid is homogeneous and isotropic.

2.2.3. Experimental setup for step-wise transient heat flux calibration. A simple apparatus is constructed in order to conduct the step-wise transient heat flux calibration (see figure 4): the FLIR SC7300L infrared camera is positioned in front of the heat transfer platform on a test bench. The image resolution matches the measurements performed in the turbine facility. A solid-state relay is connected to the heater power supply and the digital output of one of the on-board data acquisition devices. The same digital output is connected in parallel to the camera trigger, so that the power to the heater and the recording sequence can be started simultaneously with a maximum time delay between the two events of ~100 μs.

The frame rate of the camera is set to 231 frps, the maximum allowed by a full-frame acquisition, with an integration time of 100 μs and detector gain 1. 1000 frames are recorded for each sequence for a recording time of 4.33 s per sequence.

2.2.4. Data elaboration. The transient temperature increase is mapped onto a mesh of the rotor endwall by means of projective geometry (section 3.4). The temperature rise is individually evaluated for each point of the rotor endwall mesh. The linear fit between $\sqrt{t}$ and temperature rise is evaluated starting from a time $t > 2\tau_{paint}$, where τ_{paint} is the thermal diffusivity time constant of the high-emissivity coating covering the heater:

$$\tau_{paint} = \frac{d^2_{paint}}{\alpha_{paint}} \approx 9 \text{ ms} \tag{6}$$

In the presence of strong temperature gradients on the surface, lateral conduction starts occurring in the substrate. Once a sufficient amount of time has passed after turning on the power to the heater, these temperature differences start becoming relevant and the temperature rise ΔT ceases to be linear with $\sqrt{t}$. A clear example of this behaviour is given by the red curve for point B in figure 5(a). After $\sqrt{t} > 0.75\sqrt{s}$, the temperature
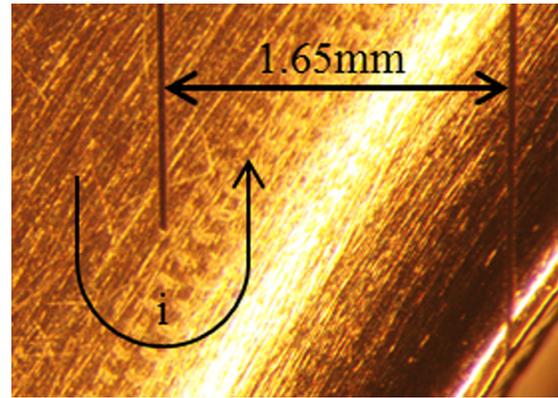

Figure 3. Detail of the laser-cut serpentine on the endwall surface.
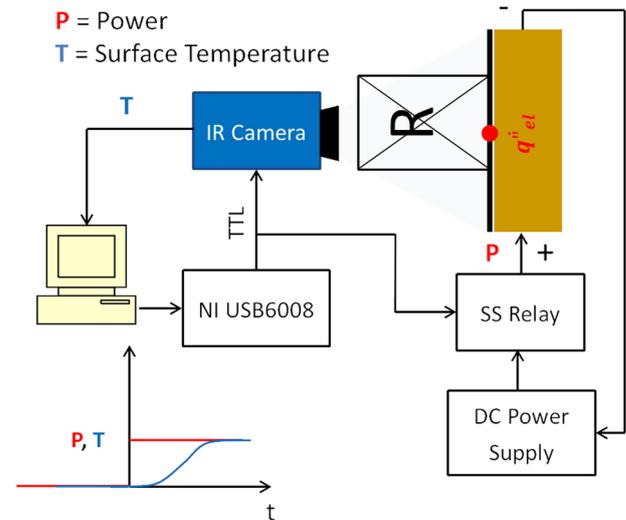

Figure 4. Schematic of step-wise transient calibration setup.

increase deviates from a linear behaviour due to heat being lost to the neighbouring region because of lateral conduction. Nonetheless, it is still possible to correctly evaluate the locally produced heat flux by restricting the analysis to the earlier portion of the curve, where lateral conduction has not yet started to significantly affect the propagation of heat within the solid and the phenomenon can still be regarded as 1D. The portion of signal to be processed to obtain a linear fit is then determined iteratively in order to minimize the root mean squared error of the fit. For each point with an rmse value exceeding 0.03 °C, points are progressively eliminated from the tail of the signal until the rmse falls below the threshold. A minimum of 10 data points are kept for the calculation of the linear fit. The result of the iterative procedure is highlighted in figure 5(a): as soon as the temperature increase deviates from the linear behaviour due to lateral conduction, the data points are discarded. A map of heat flux is obtained for the whole endwall. Non-uniformities in heat flux production up to 3 times the average value over the whole endwall are detected. Locations of heat flux non-uniformities are found not only where the turns of the tracks are because of concentrations of the streamlines of the current, but also in the central region of the heater. The reason for this can be attributed to the thickness and resistivity non-uniformities in the deposited layer.
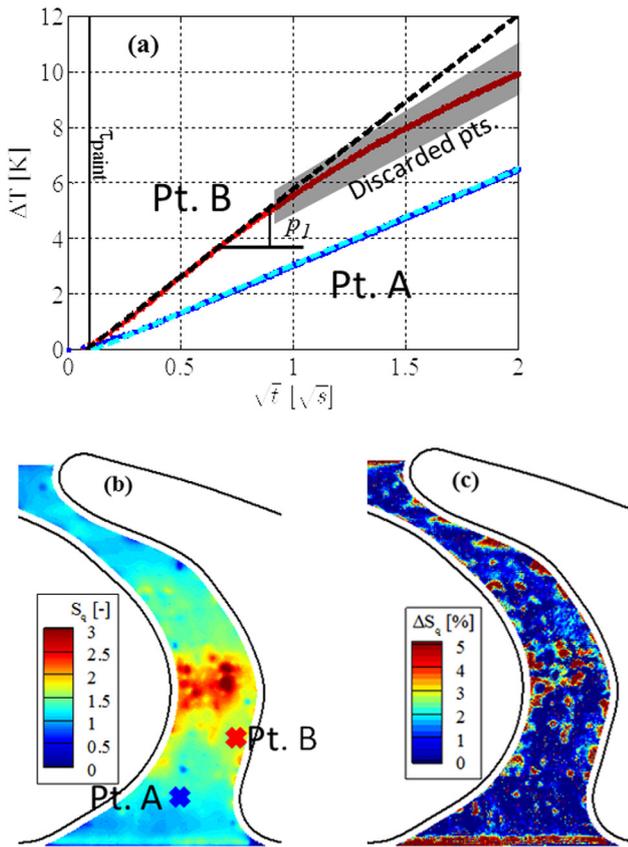
Figure 5. Surface temperature increase as a function of the square root of time (a) for points A and B marked in (b). For point B, data showing deviation from linear behaviour due to lateral conduction is discarded (shaded area). Map of (b) normalized heat flux returned by the step-wise transient calibration and (c) repeatability of the results obtained in the range 0.9–2.3 kW m^{-2}.

These are partially intrinsic to the evaporation process (section 2.2) and partially due to different annealing temperatures of the film during deposition, caused by the non-uniform temperature field in the 3D substrate (Johnson [22]).

The point-by-point scaling factor S_q is calculated as the ratio between the locally generated heat flux value and the average of this quantity over the complete passage:

$$S_q(\mathbf{x}) = \frac{\dot{q}''_{el}(\mathbf{x})}{\overline{\dot{q}''_{el}}} = \frac{\dot{q}''_{el}(\mathbf{x}) \cdot A_{ew}}{\int_{ew} \dot{q}''_{el} dA} = \frac{\frac{\sqrt{\pi}}{2} \cdot e \cdot p_1(\mathbf{x}) \cdot A_{ew}}{\frac{\sqrt{\pi}}{2} \cdot e \cdot \int_{ew} p_1 dA} = \frac{p_1(\mathbf{x})}{\overline{p_1}}$$

(7)

The scaling factor S_q multiplied by the average heat flux $\overline{\dot{q}''_{el}} = P/A_{ew}$ returns the local value of heat flux for each power level. Tests at three different levels of average heat flux, i.e. 0.9 kW m^{-2}, 1.7 kW m^{-2} and 2.3 kW m^{-2} showed the scaling factor to be independent of the power level. The average repeatability of the S_q values over the passage is within 3.7% in this heat flux range.

A typical distribution of the scaling factor is shown in figure 5(b) together with the corresponding repeatability map (figure 5(c)). Uncertainties from the fit procedures are negligible compared to the repeatability errors (one order of magnitude lower in a 95% confidence interval).

No other sources of uncertainty are considered in evaluating the global uncertainty of $S_q(\mathbf{x})$ other than repeatability and fit errors. As shown by equation (7), in fact, $S_q(\mathbf{x})$ is independent of the thermal properties of the substrate (i.e. its thermal effusivity e), hence its value is unaffected by uncertainties in the determination of e.

3. Image processing

Due to the contrasting requirements of high spatial resolution and high temperature sensitivity, the thermal imaging of a moving object (i.e. the turbine rotor endwall) in the far infrared range requires a complex image restoration procedure. Images are taken with two different detector integration times, 50 μs and 10 μs, during which the rotor moves respectively of 14.6 pixels and 2.9 pixels. The two sets are then combined into a single temperature map through the following steps:

- deblurring of the 50 μs integration time thermograms (section 3.1);
- scaling of the 10 μs integration time thermograms to match the same digital level range as the 50 μs integration time set;
- frequency analysis of the difference between the two newly obtained data sets and individuation of the characteristic frequency of the ringing introduced by deblurring;
- application of band-pass filters to the two data sets based on the frequency analysis performed at the previous point (section 3.2);
- combination of the two resulting thermograms into one hybrid data set.

A schematic overview of the image processing procedure is given in figure 6.

Each of the involved steps is described in sections 3.1 and 3.2. The uncertainty in the temperature reading resulting from the complete procedure is evaluated in section 3.3.

3.1. Deblurring of the 50 μs integration time thermograms

Smearing of edges and temperature contours is caused by the motion of the rotor during the signal integration. Analytically, any blurred image y can be represented as the convolution between a sharp image s and a blur kernel k:

$$y = k \otimes s.$$

(8)

An accelerated Richardson–Lucy [28, 29] algorithm (the built-in 'deconvblind' function of MATLAB R2013a, for details on the algorithm the reader is referred to [30] and [31]) is used to recover a maximum-likelihood estimation of s, given an initial guess of the blur kernel k, based on the measured image resolution and velocity of the rotor endwall. In the current experiment, an initial guess for the blur kernel k could be produced, as the motion of the rotor in terms of pixels is known.

The deblurring restores an isotropic image resolution of 0.32 mm/pixel. Prior to deblurring, an edge tapering treatment is applied to reduce ringing. Nonetheless, the presence
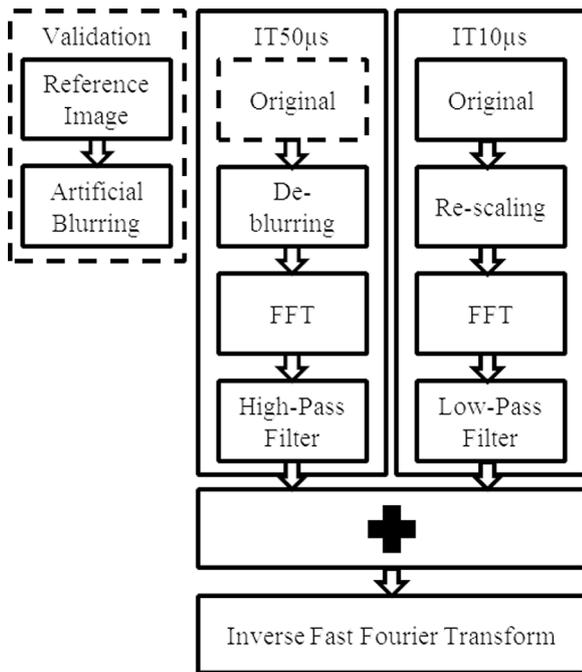
Figure 6. Schematic overview of the image reconstruction procedure. For validating the procedure the original 50 ms image is substituted with an artificially blurred version of the reference image of the still rotor.

of strong thermal gradients in the image still results in ringing patterns.

Ringing is defined as the introduction of artefacts in the reconstructed image at specific frequencies. The frequencies of the artefacts correspond to the zeros of the Fourier transform of the point-spread function [30]. As shown in figure 7(c), ringing can result in temperature oscillations of up to ~±1 °C. Band-pass filters are used to suppress this effect in the final, hybrid image (section 3.2).

3.2. Frequency-based image combination for two integration time settings

It is possible to identify the frequency range of the ringing phenomenon by studying the 2D, discrete Fourier transform of the difference between the deblurred, 50 μs integration time frame and the sharp, 10 μs integration time frame, provided that the latter is rescaled to match the digital count scale of the former. Rescaling is done on the physical grounds that the MCT detector returns a raw signal in voltage that is proportional to the absorbed radiative energy. It follows that when that the same radiative power insists on the detector, the signal is directly proportional to the integration time. This is verified experimentally by plotting the temperature readings obtained from the 10 μs integration time frame against the values in the 50 μs integration time frame (figure 8).

A linear fit is calculated for each scene.

In order to reduce the impact of noise and potential non-linearities of the analog-to-digital conversion, only the pixels corresponding to the heated endwall are considered. This is because they provide the highest well fill of the detector and

are the only ones of relevance in the frame. The fits are calculated with a 95% confidence bound.

Next, the value stored in each pixel of each 10 μs integration time thermogram is rescaled based on the calculated fit. Now the direct comparison of the 10 μs and 50 μs integration time datasets is possible. Their pixel-by-pixel difference and its 2D discrete frequency spectrum are considered for further analysis.

The rescaling of the 10 μs integration time frames artificially amplifies the raw signal and the noise, which is the main limiting factor in the accuracy of the temperature measurement at low integration times [32]. The ringing affecting the accuracy of the temperature readings in the 50 μs integration time frames occurs at much lower spatial frequencies (10–15 pixels wavelength) than the noise degrading the accuracy of the 10 μs integration time frames (1–2 pixels wavelength). It is therefore possible to apply a high pass filter to the former, thus eliminating the contribution of ringing, while applying the complementary low-pass filter to the latter, reducing the impact of noise. An image can be obtained by summing the resulting frequency spectra and inverting the discrete Fourier Transform. The appropriate size of the filter has to be chosen. This process is outlined in the validation section 3.3.

3.3. Validation of the image restoration procedure

The image restoration procedure is tested on reference images taken with a still rotor. The images are acquired with the same optical setup and acquisition parameters as during the measurements. However—differently from the ones acquired with the turbine in operation—the reference images are naturally sharp with all integration times and, in particular, even with the 50 μs integration time. The sharp 50 μs integration time frame can then be taken as the reference against which to quantify the error in temperature reading introduced by the restoration procedure. First of all, an artificially blurred frame is created from the reference by convolution with the blur kernel k (see section 3.1). The blind deconvolution algorithm is then applied to the artificially blurred frame for a variable number of iterations. A mean value of structure similarity index (MSSIM) is then calculated to quantify the resemblance of the deblurred frame to the original sharp reference. The structure similarity index (SSIM) is defined in Wang *et al* [33] as:

$$\mathrm{SSIM}(s, y_n') = \frac{(2\mu_s\mu_{y_n'} + C_1)(2\sigma_{sy_n'} + C_2)}{(\mu_s^2 + \mu_{y_n'}^2 + C_1)(\sigma_s^2 + \sigma_{y_n'}^2 + C_2)} \quad (9)$$

In the previous equation, μ_s and $\mu_{y_n'}$ respectively indicate the mean intensity of the sharp image s and the output image of the R–L algorithm at the nth iteration y_n'. σ_s and $\sigma_{y_n'}$ represent the contrast of the two images (estimated by means of their standard deviations). $\sigma_{sy_n'}$ is the correlation of the two images. The constants C_1 and C_2 ensure the stability of the calculation and their value is determined based on the dynamic range of the image. The number of iterations n_{opt} giving the maximum value of MSSIM is chosen for the processing of the measurement data. It is found that for a repeated take
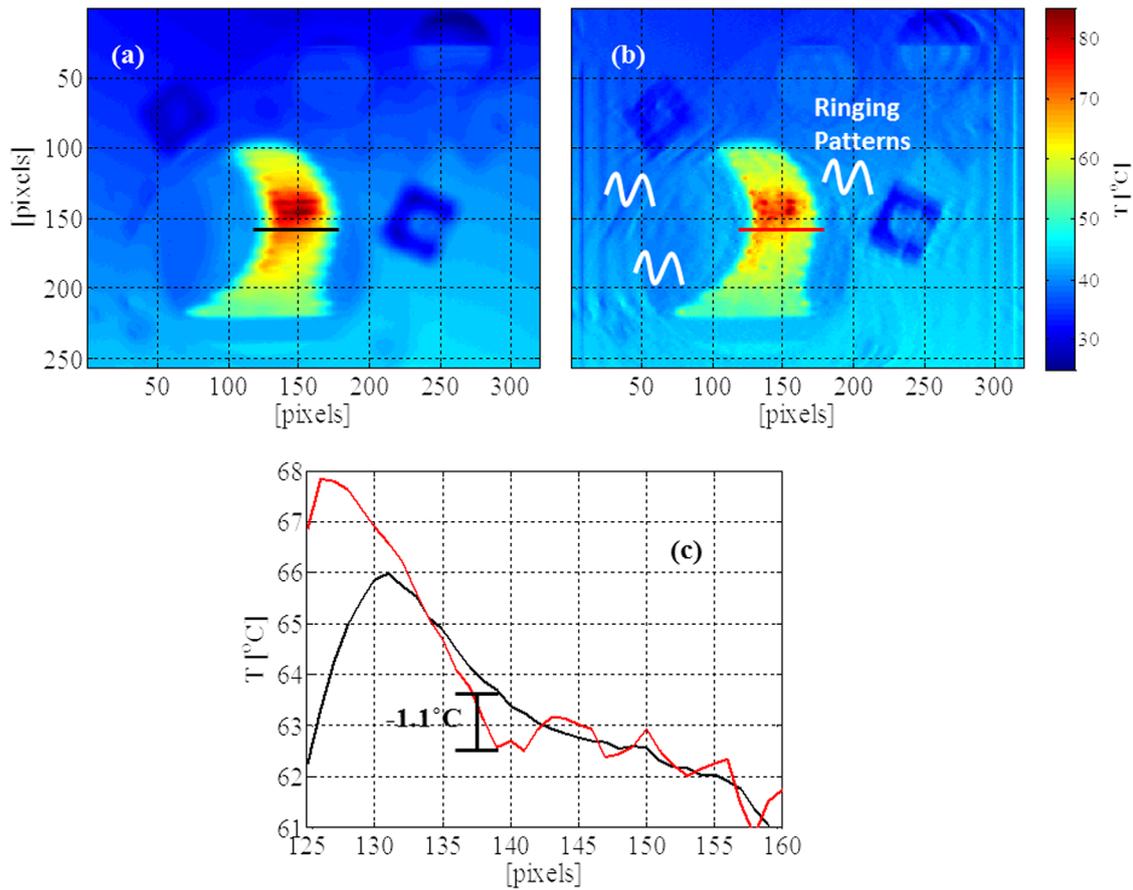
Figure 7. Original thermogram acquired with a 50 μs-long integration time (a); resulting thermogram deblurred with a blind deconvolution method. Ringing patterns are evident (b); temperature profiles extracted from the locations indicated in (a) and (b). Ringing results in oscillations of ~± 1 °C (c).
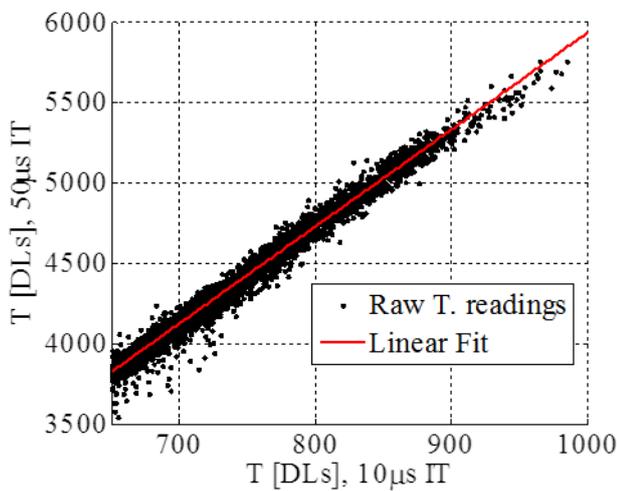

Figure 8. Temperature readings of the same scene for two different integration times (10 μs and 50 μs).

of the same frame the number of iterations maximizing the MSSIM varies by ± 1. Figure 9 shows the variation of MSSIM with the number of iterations n of the deblurring algorithm and highlights the optimal number of iterations n_{opt}.

Once the number of iterations returning the maximum value of MSSIM is identified for both camera positions, the artificially blurred frame is deblurred by blind deconvolution. The 10 μs integration time frame is rescaled as explained in section 3.2. Two complementary filters are applied to the deblurred 50 μs integration time frame and to the 10 μs integration time frame. A high-pass filter is applied to the former and a low-pass filter to the latter. The cutoff frequency is varied in the range of 0–256 pixels. The resulting spectra are summed and transformed back into an image by an inverse fast Fourier transform algorithm. The difference between the resulting hybrid image and the reference image taken with a 50 μs integration time is evaluated in terms of root mean square error over the region of interest highlighted in figure 10(a).

For each view, the root mean square error can be minimized by choosing an appropriate cutoff wavelength for the two filters. The optimal cutoff wavelength is the one separating the power spectrum of figure 11(b) into two portions respectively containing 10% (low-pass filter) and 90% of the power (high-pass filter). For the example of figures 10 and 11, the cutoff wavelength is 87 pixels. The minimization of the root mean square error with respect to the 50 μs integration time image of the still rotor is shown in figure 10(b). For the uncertainty
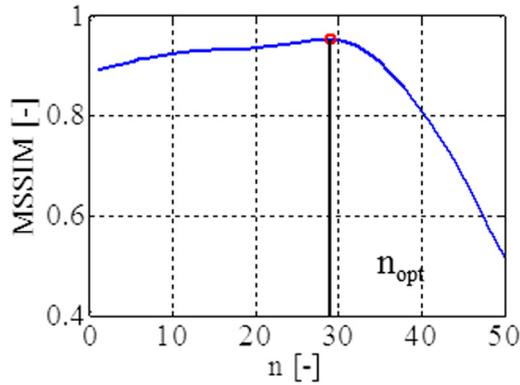
Figure 9. Mean structure similarity index variability with number of iterations of the blind deconvolution algorithm for a typical frame. The maximum value is highlighted in red.

analysis, the error in the surface temperature is conservatively assumed to be $\pm 0.46\,\mathrm{K}$, which is the highest obtained for all positions considered.

3.4. Geometrical reconstruction of Images

The image reconstruction tools developed by Laveau [19] and based on the theory of projective geometry as described in [34] are adapted to the geometry of the rotor components. The reader is referred to these works for further details. Points of lower emissivity are drawn on the black coating on the hub endwall surface with silver ink as a means of referencing the thermograms to the CAD model of the turbine (see figure 2(b)). Digital pictures of the PEEK platforms painted and marked were acquired as geometrical reference. An algorithm compares the 3D coordinates of reference points extracted from a CAD model of the platform-jig assembly with the points of the 2D digital pictures selected by the user. A geometrical transformation is obtained and used to reconstruct the 3D coordinates of the IR markers in the CAD frame of reference. The coordinates obtained are used to calculate the geometrical transformation relating the thermograms acquired during the measurements to the 3D CAD model of the rotor hub endwall.

4. Experimental results from measurements in the axial turbine research facility LISA

4.1. LEC's rotating axial turbine research facility LISA

The experiments were performed using the research turbine facility at the Laboratory for Energy Conversion (LEC) at ETH Zurich. A schematic view of the experimental facility is given in figure 12. The air loop of the facility is quasi-closed and includes a radial compressor, a two-stage water-to-air heat exchanger and a calibrated Venturi nozzle for mass flow measurements. At the exit of the compressor, the air is directed through a set of heat exchangers that control the turbine inlet total temperature $T_{t,\mathrm{in}}$ to an accuracy of $\pm 0.2\,\mathrm{K}$. A 3 m long flow conditioning stretch ensures a homogeneous flow field at the turbine inlet. Additionally, the flow undergoes acceleration ahead of the turbine section in order to reduce the significance of remaining flow non-uniformities from upstream.
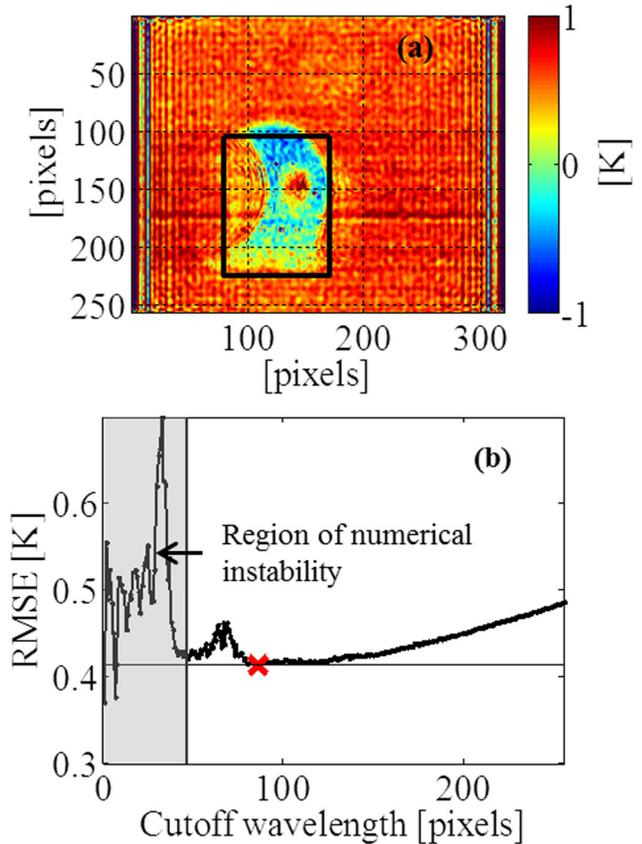

Figure 10. Temperature difference between hybrid image generated with filters with cutoff wavelength of 87 pixels and reference image. The region of interest is highlighted with a black rectangle (a); root mean square error in temperature over the region of interest as a function of the cutoff wavelength of the filters (b).

The power available on the shaft is then transmitted to a DC generator via a gearbox. The generator absorbs the turbine power and controls the rotational speed with an accuracy of $\pm 0.02\%$ ($\pm 0.5\,\mathrm{rpm}$). A torque meter installed on the vertical shaft between the turbine and the gearbox measures the torque on the rotor shaft. At the exit of the test section, two successive rows of deswirl vanes help to recover the static pressure before going through the Venturi nozzle and back to the compressor.

A 1.5 stage high work turbine configuration is installed in the test section of the facility. Each aerofoil has a complex 3D geometry optimized for minimizing the aerodynamic losses. The turbine facility is primarily used for aerodynamic measurements and stage performance assessment, but Laveau *et al* [19] have also performed heat transfer measurements on stationary parts. More details on the rig and the aerodynamic measurement techniques can be found in Schüpbach [35] and Mansour [36].

Heat transfer quantities are measured for two turbine operating conditions, summarized in table 1. The results are presented in terms of Nusselt number Nu and non-dimensional adiabatic wall temperature Θ, respectively defined as:

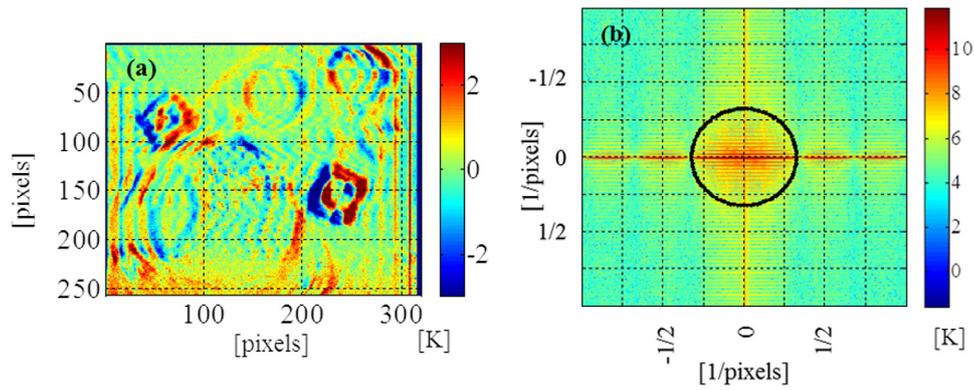$$\mathrm{Nu} = \frac{h \cdot C_{\mathrm{ax}}}{\kappa_{\mathrm{air}}} \qquad (10)$$

Figure 11. Temperature differences between the rescaled 10 μs integration time frame and the deblurred 50 μs integration time frame. Fluctuations are in the order of ± 1.5 °C (a). 2D discrete frequency spectrum of (a). The black circle indicates the 10% power threshold used to identify the size of the frequency filter (b).

$$\Theta = (T_{ad} - T_{t,rel}) / \frac{v_{\infty,in}^2}{2 \cdot C_{p,in}} \qquad (11)$$

In equation (10), C_{ax} is the axial chord of the rotor blade at midspan, κ_{air} is the thermal conductivity of air.

In equation (11), T_{ad} is the adiabatic wall temperature, $T_{t,rel}$ is the relative total temperature at rotor inlet, $v_{\infty,in}$ is the mass-averaged relative flow velocity at rotor inlet and $C_{p,in}$ is the specific heat of air. All air properties are evaluated at the mass-averaged static conditions measured at rotor inlet.

The measurements cover the inlet portion of the passage for 70% of the global hub endwall surface area.

4.2. Data acquisition

Data was acquired for two of the turbine's operating conditions: the rated operating condition (or design point) and an off-design condition (see table 1). Compared to the design point, the off-design condition presents a lower mass flow rate with identical rotational speed and total inlet temperature. This results in a negative incidence on the rotor blade of about 12.3° at mid-span.

Once a steady operation of the turbine and the thermal steady state of the platform is reached, data is acquired for 4 levels of average heat flux produced by the heating film, ranging between 1.7 kW m^{-2} $\pm$ 1.6%–9.9 kW m^{-2} $\pm$ 0.7%. The camera acquisition is synchronized to the rotation of the turbine's shaft by means of an optical trigger. The delay of the frame acquisition with reference to the TTL signal of the turbine's shaft is set so that the platform is centred between the wakes of the upstream stator when its surface temperature is recorded. The inlet portion of the passage until 60% of the axial chord is imaged by positioning the infrared camera at two angles (90° and 75°) with reference to the turbine axis. Each recorded sequence consists of 1000 infrared frames. A sequence is recorded for each of the two camera positions, with two detector integration times: 10 μs and 50 μs. A total of 16000 frames is acquired per test case.

Contemporarily, the temperature of the PEEK substrate is recorded by 9 PT100 RTDs embedded 1 mm below the

surface. Their signal is recorded by the Wi-Fi controlled, on-board data acquisition system installed on the blisk (section 2). The temperature reading is then used to estimate the conduction losses in the substrate (see section 4.4.2).

4.3. Heat transfer quantities calculation

Similarly to what summarized in [19], the equations used for the calculation of the heat transfer quantities (heat transfer coefficient h and adiabatic wall temperature T_{ad}) are:

$$\dot{q}''_{el} - \dot{q}''_{cond} - \dot{q}''_{rad} = \dot{q}''_{conv} \qquad (12)$$

$$\dot{q}''_{el} = S_q \frac{P}{A_{ew}} \qquad (13)$$

$$\dot{q}''_{cond} = \frac{\kappa_{sub}}{D}(T_w - T_{sub}) \qquad (14)$$

$$\dot{q}''_{conv} = h(T_w - T_{ad}) \qquad (15)$$

$$\dot{q}''_{rad} = \varepsilon\sigma(T_w^4 - T_{amb}^4) \qquad (16)$$

The convective heat flux $\dot{q}''_{conv}$ is calculated from the energy balance (12), after having determined all of the contributions on the left side of the equation. In particular, in equation (13), the electrical heat flux generated by the serpentine is calculated based on the electrical power P fed to the heater, the surface area A_{ew} of the heater and the scaling factor S_q measured as described in section 2.2.1. The wall temperature T_w in equations (14)–(16) is measured with the infrared camera. The reference temperature T_{amb} for the calculation of the radiative losses in equation (16) is assumed to be the total relative rotor inlet temperature.

The heat transfer quantities h and T_{ad} are determined with a point-wise linear fit of the wall temperature versus the convective heat flux, as shown in figure 13.

4.4. Uncertainty analysis

The uncertainty in the determination of the heat transfer quantities, i.e. heat transfer coefficient and adiabatic wall temperature essentially propagates from:
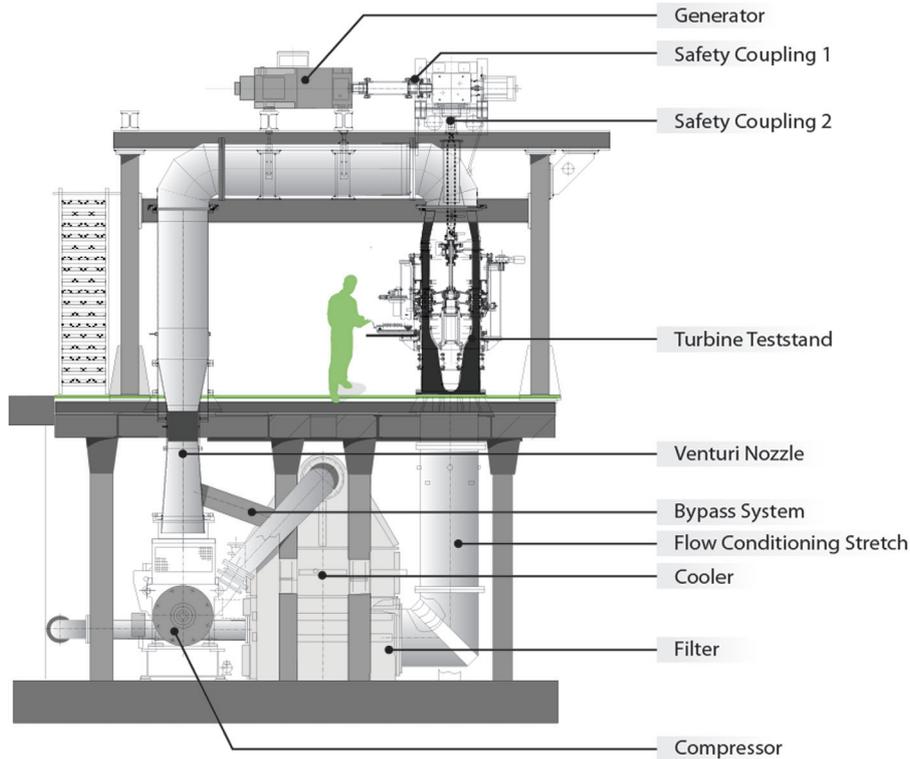
Figure 12. Schematic of the rotating axial turbine facility LISA, Laboratory for Energy Conversion, ETH Zurich.

Table 1. Operating conditions of the LISA research turbine during the experiments

	Case 1: design point	Case 2: off-design condition
Total rotor relative inlet temperature $T_{t,\text{in}}$	(313.8 ± 0.3) K	(317.2 ± 0.3) K
Stage pressure ratio	$1.65 \pm 0.4\%$	$1.33 \pm 0.4\%$
Reynolds number R exit-ReCax	570 k	310 k
Rotor speed	(2700 ± 0.5) rpm	(2700 ± 0.5) rpm
Mass flow	$11.7 \,\text{kg s}^{-1}$	$8.3 \,\text{kg s}^{-1}$
Injection ratio	$(0.8 \pm 0.01)\%$	$(0.8 \pm 0.01)\%$

Figure 13. The linear fit procedure is illustrated for specific points in the passage, the heat transfer coefficient h is given by the slope of the fit, while the adiabatic wall temperature T_{ad} by the intercept. Locations 1–4 of the passage for which the fit is performed are indicated in figure 15.

- errors in the determination of the electrical heat flux provided at the endwall (section 4.4.1);
- errors in the determination of the conductive losses through the insulating substrate (section 4.4.2);
- errors in the determination of the endwall temperature (0.46 K, see section 3.3).

The overall uncertainty on Nusselt number and non-dimensional adiabatic wall temperature is evaluated by successively perturbing the relevant inputs by their respective uncertainties using Moffat's [37] method.

4.4.1. Errors in the determination of the electrical heat flux provided at the endwall. Based on equation (11), errors in the estimation of the electrical heat flux provided by the film heater of the platform propagate from the uncertainties in the power readings and the scaling factor measured in section 2.2 to account for non-uniformities.
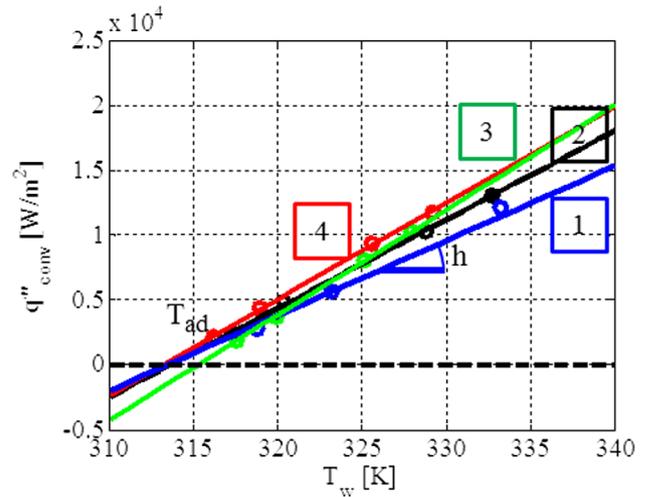
Errors in the surface area are neglected as the platforms are manufactured with tolerances within ± 50 μm over a nominal surface area of the endwall greater than $1300 \,\text{mm}^2$, corresponding to an error of less than 200 ppm.

The relative error on the electrical heat flux can be quantified as:

$$\frac{\delta \dot{q}''_{\text{el}}}{\dot{q}''_{\text{el}}} = \frac{\delta S_{\text{q}}}{S_{\text{q}}} + \frac{\delta P}{P} \qquad (17)$$

The highest uncertainties in power *P* are detected for the highest power level (1.56% at 13 W). This uncertainty level, summed to the local uncertainty in value of the scaling factor S_q (figure 5(b)), results in an average uncertainty of 5.3% over the whole passage. The uncertainty in electrical heat flux is the second most relevant contributor to the overall uncertainty (22% of the overall uncertainty) after that coming from the conduction loss estimation (70% of the overall uncertainty).

4.4.2. Errors in the determination of the conductive losses through the insulating substrate. The local conductive heat loss is evaluated based on the readings of the 9 PT100 RTDs and the thermal properties of the substrate according to equation (11), where T_w is the wall temperature measured at the normal projection on the endwall of the PT100 location and T_{sub} is the substrate temperature read by the PT100 thermometer. For each heat flux level, an average value of conductive loss is calculated over the passage and used in the energy balance (9). The average values fall between 1.6% and 6.8% for the nominal operating point and between and 11.2% and 18.7% for the off-design condition. For a conservative estimation of the uncertainty, the conduction losses are varied up to double of the value recorded for both cases when applying Moffat's [37] perturbation method.

Overall, the average uncertainty on the Nusselt number value over the whole passage is 9.0% and 0.35 K on the adiabatic wall temperature. The final uncertainty distributions for the nominal operating condition are shown in figure 14.

4.5. Results

Results are shown for the two operating conditions summarized in table 1, i.e. the rated operating condition for the examined turbine and an off-design condition with a reduced pressure ratio (1.33 instead of 1.65) and mass flow rate (8.5 kg s^{-1} instead of 11.65 kg s^{-1}).

The change of these two operating parameters affects the results because of the consequent Reynolds number reduction and the negative incidence of the flow on the rotor blades ($\sim$−12.3°).

Both sets of results show the following expected features in the Nusselt number distributions (figures 15(a) and 16(a)):

- the start of the thermal boundary layer at the very front of the passage. This derives from the fact that the heated endwall begins at this axial location;
- a high heat transfer region towards the leading edge and pressure side of the blade, which is attributed to the presence of the stagnation point and the formation of the pressure side leg of the horseshoe vortex;
- a triangular region where the heat transfer coefficient is lower towards the inlet, downstream of the start of the thermal boundary layer;
- the increase in heat transfer due to the flow acceleration going towards the throat of the passage.

Similar observations have been reported in literature for studies performed in linear cascades (Blair [38], Graziani *et al* [24], Goldstein *et al* [39]).
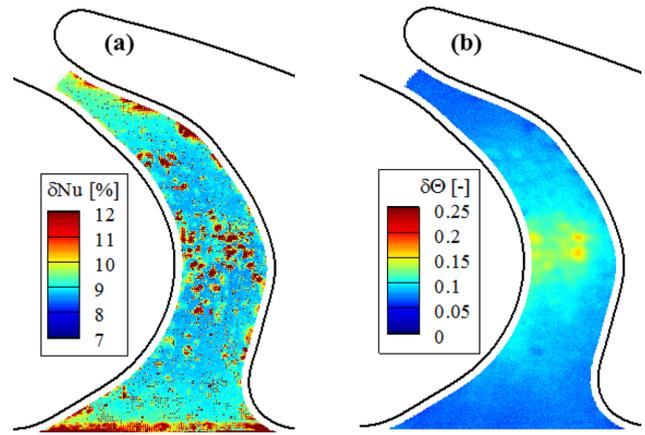

Figure 14. Overall uncertainty in Nusselt number (a) and in non-dimensional adiabatic wall temperature (b) for the nominal operating condition.
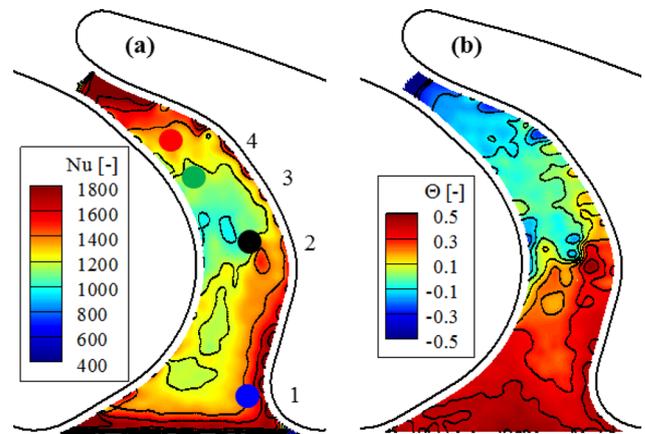

Figure 15. Nusselt number distribution for design condition and injection ratio 0.8% (a). Adiabatic wall temperature referred to the total relative rotor inlet temperature for design conditions and injection ratio 0.8% (b).
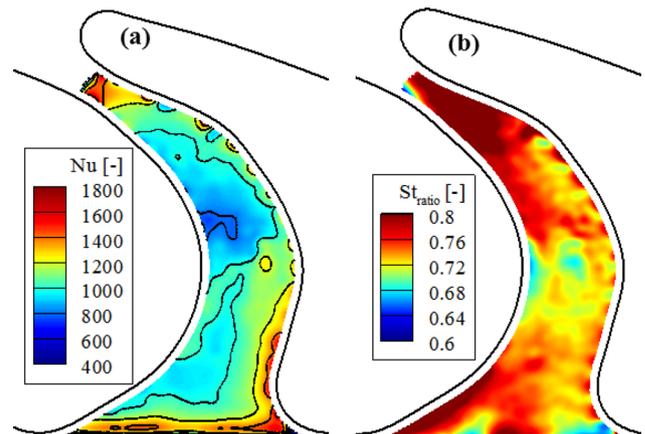

Figure 16. Nusselt number distribution for off-design condition and injection ratio 0.8% (a) ratio of Stanton number between design and off-design operating condition (b).

Additionally, a region of lower heat transfer is observed between ~40 and ~60% of the axial extent of the passage. This is attributed to the detachment of the rotor hub passage vortex from the endwall and its migration to higher radial locations.
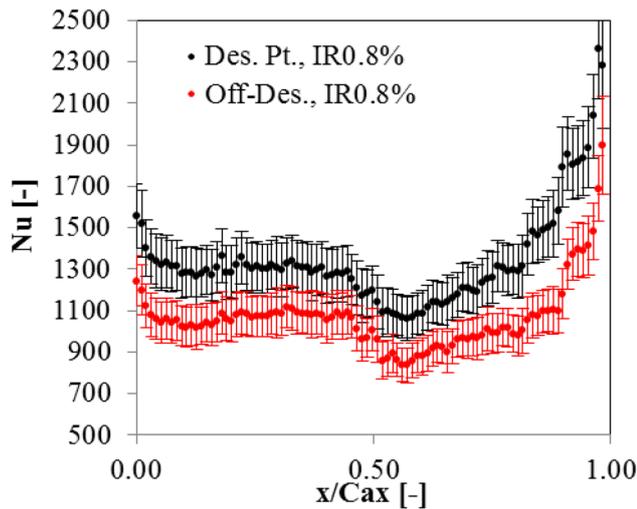
Figure 17. Laterally averaged Nusselt number profiles for design point and off-design operating condition.

This behaviour is consistent with what typically observed in studies concerning rotor secondary flows such as Regina *et al* [40], Jenny *et al* [41] and Ong *et al* [42]. Unsteady aerodynamic data collected on the same turbine configuration confirm the radial migration of the rotor hub secondary flows up to 40% of the span (Schädler *et al* [43]). The low heat transfer level in the region is then explained by the presence of low-momentum fluid in the wake of the detaching hub passage vortex.

The flow acceleration and expansion is evident in the distribution of non-dimensional adiabatic wall temperature for the design point (figure 15(b)).

A comparison between the cases is shown as a ratio of Stanton numbers in figure 16(b). The ratio is defined as:

$$St_{ratio} = \frac{St_{Des.\ Pt.}}{St_{Off-Des.}} \tag{18}$$

Based on the turbulent correlation for a flat plate with uniform heat flux [44] it is possible to calculate:

$$St_{ratio} \approx \left(\frac{Re_{Des.\ Pt.}}{Re_{Off-Des.}} \right)^{-0.2} = 0.9 \tag{19}$$

based on the Reynolds numbers calculated at rotor exit as reported in table 1. The values of St_{ratio} shown in figure 16(b) approach this estimate at the throat of the passage.

Consistently, the laterally averaged profiles in figure 17 show a decrease of Nusselt number beyond the uncertainties.

5. Conclusions

A novel experimental technique has been developed to measure, with high resolution (0.32 mm/pixel by 0.32 mm/pixel), the heat load on the endwall of a moderate speed rotating axial turbine research facility. The following specific developments were introduced to accomplish the measurements:

- a highly accurate and versatile manufacturing technique for film heaters on surfaces with complex shapes. The

process is applicable to virtually any endwall geometry from axisymmetric to aggressively contoured;
- quantitative infrared image reconstruction tools enabling deblurring and frequency based image combination;
- a step-wise transient heat flux calibration for film heaters with arbitrary heat flux distribution. The calibration allows accurate measurement of the local non-uniformities (errors <3.7%) and allows heat transfer measurements with uncertainties <10% on heat transfer coefficient and 0.35 K on adiabatic wall temperatures even in the presence of non-uniform thermal boundary conditions;

Measurements were performed as a proof of concept. The results present physical trends related to flow features typical of a turbine passage and are consistent with changes in operating condition, thus demonstrating the sensitivity of the technique.

References

[1] Meola C and Carlomagno G M 2004 Recent advances in the use of infrared thermography *Meas. Sci. Technol.* **15** R27
[2] Carlomagno G M and Cardone G 2010 Infrared thermography for convective heat transfer measurements *Exp. Fluids* **49** 1187–218
[3] Scherer V, Wittig S, Bittlinger G and Pfeiffer A 1993 Thermographic heat transfer measurements in separated flows *Exp. Fluids* **14** 17–24
[4] Schulz A 2000 Infrared thermography as applied to film cooling of gas turbine components *Meas. Sci. Technol.* **11** 948
[5] Cardone G, Astarita T and Carlomagno G 1997 Heat transfer measurements on a rotating disk *Int. J. Rotat. Mach.* **3** 1–9
[6] Lyons O, Murray D and Torrance A 2008 Air jet cooling of brake discs *Proc. Inst. Mech. Eng.* C **222** 995–1004
[7] Siroux M, Harmand S and Desmet B 2002 Experimental study using infrared thermography on the convective heat transfer of a TGV brake disk in the actual environment *Opt. Eng.* **41** 1558–64
[8] Astarita T, Cardone G and Carlomagno G 2002 Spiral vortices detection on a rotating disk *Proc. of 23rd Congress Int. Council Aeronautical Sciences, Paper n.* ICAS2002-3.6
[9] Astarita T and Cardone G 2008 Convective heat transfer on a rotating disk with a centred impinging round jet *Int. J. Heat Mass Transfer* **51** 1562–72
[10] Dunn M G 2001 Convective heat transfer and aerodynamics in axial flow turbines *J. Turbomach.* **123** 637–86
[11] Blair M F 1992 An experimental study of heat transfer in a large-scale turbine rotor passage *ASME 1992 Int. Gas Turbine and Aeroengine Congress and Exposition* p V004T09A012
[12] de la Loma A, Paniagua G, Verrastro D and Adami P 2008 Transonic turbine stage heat transfer investigation in presence of strong shocks *J. Turbomach.* **130** 031019
[13] Abhari R, Guenette G, Epstein A and Giles M 1991 Comparison of time-resolved turbine rotor blade heat

transfer measurements and numerical calculations *ASME 1991 Int. Gas Turbine and Aeroengine Congress and Exposition* p V004T09A018

[14] Dunn M G, Rae W J and Holt J L 1984 Measurement and analyses of heat flux data in a turbine stage: part I—description of experimental apparatus and data analysis *J. Eng. Gas Turbines Power* **106** 229–33

[15] Dunn M G, Rae W J and Holt J L 1984 Measurement and analyses of heat flux data in a turbine stage: part II—discussion of results and comparison with predictions *J. Eng. Gas Turbines Power* **106** 234–40

[16] Moffat R J 1998 What's new in convective heat transfer? *Int. J. Heat Fluid Flow* **19** 90–101

[17] Rogalski A 2008 New material systems for third generation infrared photodetectors *Opto-electron. Rev.* **16** 458

[18] Lynch S P, Sundaram N, Thole K A, Kohli A and Lehane C 2011 Heat transfer for a turbine blade with nonaxisymmetric endwall contouring *J. Turbomach.* **133** 011019

[19] Laveau B, Abhari R S, Crawford M E and Lutum E 2014 High resolution heat transfer measurements on the stator endwall of an axial turbine *J. Turbomach.* **137** 041005

[20] Laveau B, Abhari R S, Crawford M E and Lutum E 2015 High resolution heat transfer measurement technique on contoured endwall with non-uniform thermal resistance *ASME Turbo Expo 2015: Turbine Technical Conf. and Exposition* p V05BT13A023

[21] Ochs M, Horbach T, Schulz A, Koch R and Bauer H 2009 A novel calibration method for an infrared thermography system applied to heat transfer experiments *Meas. Sci. Technol.* **20** 075103

[22] Johnson B 1990 Electrical resistivity of copper and nickel thin-film interconnections *J. Appl. Phys.* **67** 3018–24

[23] O'Dowd D O, Zhang Q, He L, Ligrani P M and Friedrichs S 2011 Comparison of heat transfer measurement techniques on a transonic turbine blade tip *J. Turbomach.* **133** 021028

[24] Graziani R, Blair M F, Taylor J and Mayle R 1980 An experimental study of endwall and airfoil surface heat transfer in a large scale turbine blade cascade *J. Eng. Power* **102** 257–67

[25] Simonich J C and Moffat R J 1982 New technique for mapping heat-transfer coefficient contours *Rev. Sci. Instrum.* **53** 678–83

[26] Baughn J, Takahashi R, Hoffman M and McKillop A 1985 Local heat transfer measurements using an electrically heated thin gold-coated plastic sheet *J. Heat Transfer* **107** 953–9

[27] Gustafsson S E, Karawacki E and Khan M N 1979 Transient hot-strip method for simultaneously measuring thermal conductivity and thermal diffusivity of solids and fluids *J. Phys. D: Appl. Phys.* **12** 1411

[28] Lucy L B 1974 An iterative technique for the rectification of observed distributions *Astron. J.* **79** 745

[29] Richardson W H 1972 Bayesian-based iterative method of image restoration *JOSA* **62** 55–9

[30] Hanisch R J, White R L and Gilliland R L 1996 Deconvolution of Hubble space telescope images and spectra *Deconvolution of Images and Spectra* 2nd edn, ed A J Peter (New York: Academic) pp 310–60

[31] Biggs D S and Andrews M 1997 Acceleration of iterative image restoration algorithms *Appl. Opt.* **36** 1766–75

[32] Jones R C 1953 Performance of detectors for visible and infrared radiation *Advances in Electronics and Electron Physics* vol 5, ed L Marton (New York: Academic) pp 1–96

[33] Wang Z, Bovik A C, Sheikh H R and Simoncelli E P 2004 Image quality assessment: from error visibility to structural similarity *IEEE Trans. Image Process.* **13** 600–12

[34] Faugeras O, Luong Q-T and Papadopoulo T 2004 *The Geometry of Multiple Images: the Laws That Govern the Formation of Multiple Images of a Scene and Some of Their Applications* (Cambridge, MA: MIT press)

[35] Schuepbach P, Abhari R S, Rose M G, Germain T, Raab I and Gier J 2010 Effects of suction and injection purge-flow on the secondary flow structures of a high-work turbine *J. Turbomach.* **132** 021021

[36] Mansour M, Chokani N, Kalfas A I and Abhari R S 2011 Impact of time-resolved entropy measurement on a one-and-one-half-stage axial turbine performance *J. Turbomach.* **134** 021008

[37] Moffat R J 1988 Describing the uncertainties in experimental results *Exp. Therm. Fluid Sci.* **1** 3–17

[38] Blair M 1974 An experimental study of heat transfer and film cooling on large-scale turbine endwalls *ASME 1974 Int. Gas Turbine Conf. and Products Show* p V01AT01A033

[39] Goldstein R J and Spores R A 1988 Turbulent transport on the endwall in the region between adjacent turbine blades *J. Heat Trans.* **110** 862–69

[40] Regina K, Kalfas A I and Abhari R S 2014 Experimental Investigation of purge flow effects on a high pressure turbine stage *J. Turbomach.* **137** 041006

[41] Jenny P, Abhari R S, Rose M G, Brettschneider M, Engel K and Gier J 2013 Unsteady rotor hub passage vortex behavior in the presence of purge flow in an axial low pressure turbine *J. Turbomach.* **135** 051022

[42] Ong J, Miller R J and Uchida S 2012 The effect of coolant injection on the endwall flow of a high pressure turbine *J. Turbomach.* **134** 051003

[43] Schädler R, Kalfas A I, Abhari R S, Schmid G, auf dem Kampe T and Prabhu S B 2017 Novel high-pressure turbine purge control features for increased stage efficiency *GPPF 2017*

[44] Kays W M, Crawford M E and Weigand B 2012 *Convective Heat and Mass Transfer* (New York: McGraw-Hill)